

Investigation of Geogrid-Reinforced Railroad Ballast Behavior Using Large-Scale Triaxial Testing and Discrete Element Modeling

Debakanta Mishra, Yu Qian, Hasan Kazmee, and Erol Tutumluer

Geogrids are well known for improving the performance of unbound aggregate layers in transportation applications by providing confinement and restraining movement through interlock between individual aggregate particles and geogrid apertures. Geogrid reinforcement offers an effective remedial measure when railroad track structures are susceptible to track geometry defects resulting from excessive movement and particle reorientation within the ballast layer. This paper presents findings from an ongoing research study at the University of Illinois aimed at quantifying the effects of geogrid reinforcement on the shear strength behavior of railroad ballast. The effects of two geogrid types on ballast shear strength were evaluated through laboratory testing and numerical modeling. An imaging-based discrete element method (DEM) modeling approach was used to identify the optimal position for geogrid reinforcement to achieve the maximum shear strength gain in cylindrical triaxial specimens. Geogrids were installed at five depths within the cylindrical specimen and tested for shear strength properties with a large-scale triaxial test setup to evaluate the effectiveness of both geogrid aperture shape and reinforcement depth. Placing two layers of geogrids in the middle of the specimen was found to result in the maximum shear strength gain. Such placement of the geogrid ensured the intersection of the shear failure plane with the reinforcement layer, ultimately leading to significant shear strength gains. The DEM simulations were observed to capture accurately the ballast shear strength behavior with and without geogrid reinforcement.

Geogrids have been commonly used in highway and unpaved road applications to improve the pavement system performance through their interlocking ability of individual aggregate particles. In the case of railroad track applications, geogrids can be placed both within the subballast and ballast layers. The reinforcement application in ballast layer improves strength and modulus properties of the ballast layer, limits lateral movement of aggregate particles, and reduces vertical settlement through effective geogrid–aggregate interlocking. Walls and Galbreath reported geogrid reinforcement to have the potential to reduce the frequency of ballast maintenance operations

by as much as 12 times (1). The placement of geogrid within the ballast layer is often dictated by the length of tamping tines, with the primary objective being to prevent damage to the geogrid layer during tamping operations. Optimal positioning of geogrids within the ballast layer to maximize its effectiveness in limiting lateral movement of particles and reducing vertical settlement has not been thoroughly studied.

Many types of geogrids are available in the market with different aperture shapes and sizes, rib thicknesses, and mechanical properties. Because the primary benefits of geogrid reinforcement are derived from interlocking between geogrid ribs and aggregates, geogrid aperture shape and size as well as rib thickness have been identified as important factors governing the effectiveness of geogrid reinforcement on unbound aggregate layer performance (2). The aperture shapes of geogrids can be square, rectangular, or triangular. Geogrids with square or rectangular apertures are often referred to as biaxial geogrids, because their tensile strength and stiffness values are mobilized mainly along two directions (i.e., machine and cross-machine directions). Several studies have used laboratory experiments and numerical simulations to establish the effectiveness of biaxial geogrids for improving bearing capacity of the railroad track substructure (3–6). More recently, geogrids with triangular-shaped apertures have also been developed with the claims to provide more uniform reinforcement in all directions. An early work on comparative evaluation of the reinforcement benefits of geogrids with rectangular and triangular apertures used discrete element modeling simulations of large-scale direct shear tests (7). Recent research efforts have also focused on evaluating performance improvements of triangular geogrid-reinforced transportation systems (8, 9). Dong et al. compared the performances of triangular- and rectangular-aperture geogrids using both numerical and experimental methods (10).

Depending on the type of application, different aperture shapes and sizes have been proposed by researchers to maximize the effects of geogrid reinforcement. For example, McDowell et al. used the discrete element method (DEM) to propose a ratio of 1.4 between geogrid aperture size and ballast particle diameter to achieve optimum performance (11). Accordingly, for a ballast material with 50-mm maximum particle size, the desired aperture size of ballast should be 70 mm (2). Although several research studies have investigated the effects of geogrid placement depth on ballast performance (2, 5), no significant effort has focused on optimizing the position of geogrid reinforcement in the ballast layer through large-scale triaxial shear strength testing. This paper presents findings from an ongoing research study at the University of Illinois focusing on triaxial testing

Department of Civil and Environmental Engineering, University of Illinois at Urbana-Champaign, 205 North Mathews Avenue, Urbana, IL 61801. Corresponding author: E. Tutumluer, tutumlue@illinois.edu.

Transportation Research Record: Journal of the Transportation Research Board, No. 2462, Transportation Research Board of the National Academies, Washington, D.C., 2014, pp. 98–108.
DOI: 10.3141/2462-12

of geogrid-reinforced ballast specimens using a large-scale triaxial test device and modeling the micromechanical interlock behavior of geogrid–aggregate systems using the DEM. Two geogrid types with triangular- and square-aperture shapes were placed at different positions along the depth of cylindrical triaxial specimens to evaluate their effects on ballast shear strength. An imaging-based ballast DEM modeling approach has been used to simulate the laboratory test results.

OBJECTIVE AND SCOPE

The primary objective of this research effort was to identify the optimal position for geogrid placement in a ballast triaxial test specimen for maximizing the shear strength properties. This objective was accomplished by triaxial testing and imaging-based DEM modeling to evaluate the reinforcement benefits through increased shear strength properties. The image-aided DEM approach creates actual ballast aggregate particles as three-dimensional polyhedral elements and simulates large-scale triaxial shear strength tests. A novel approach was adopted to monitor the radial deformations at different positions along the specimen length to identify locations that undergo the maximum lateral expansion during the shearing process. This information was then used to design five reinforcement configurations, representing different positions of geogrid placement along the specimen length. Large-scale monotonic triaxial shear strength testing was conducted on specimens corresponding to the five reinforcement configurations, using two types of geogrid. Results from the laboratory tests were used to identify the most important factors governing the effects of geogrid reinforcement on shear strength increase. The geogrid-reinforced ballast specimen

behavior could be adequately simulated using the DEM approach. Both the triaxial strength tests and the DEM simulation results are presented in this paper to evaluate the reinforcement benefits and document mechanisms governing behavior of the ballast specimens reinforced with different aperture geogrids placed at different positions along the specimen depth.

PROPERTIES OF BALLAST MATERIAL USED

The ballast material used in this study was a clean limestone aggregate having 100% crushed particles. Figure 1 shows the particle size distribution of the ballast material that adequately met the U.S. American Railway Engineering and Maintenance-of-Way Association No. 24 gradation requirements. Ballast particles corresponding to different sieve sizes were scanned using the University of Illinois Aggregate Image Analyzer (12) to establish imaging-based morphological indexes, such as the flat and elongated ratio, the angularity index, and the surface texture index (13). These imaging-based morphological indexes were subsequently used to generate ballast aggregate particle shapes as three-dimensional (3-D) polyhedrons to be used in the DEM simulations.

TRIAXIAL SHEAR STRENGTH TESTING OF RAILROAD BALLAST

A large-scale triaxial test device (University of Illinois Triaxial Ballast Tester or TX-24), recently developed at the University of Illinois for testing specifically ballast-size aggregate materials, was used for conducting the shear strength tests on unreinforced

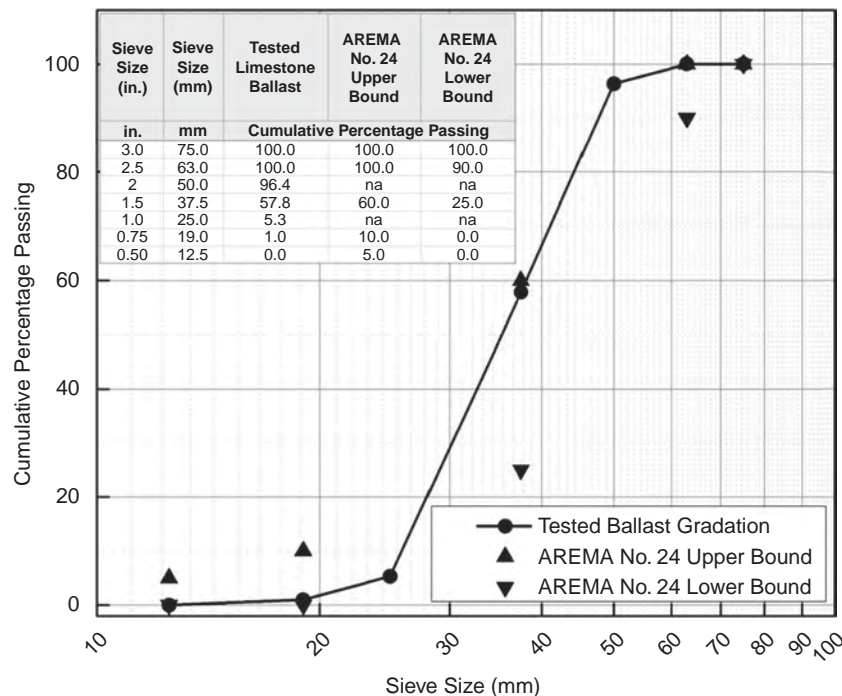


FIGURE 1 Particle size distribution of the limestone ballast used in the current study (AREMA = American Railway Engineering and Maintenance-of-Way Association; no. = number; na = not applicable).

and geogrid-reinforced ballast specimens. By testing specimens with dimensions of 305 mm (12 in.) in diameter and 610 mm (24 in.) in height, the TX-24 test setup presents unique capabilities to experimentally evaluate the shear strength, resilient modulus, and permanent deformation characteristics of railroad ballast materials. Further details on different components of this test equipment have been provided elsewhere (14).

The procedure explained by Mishra et al. was used to prepare cylindrical specimens, 305 mm (12 in.) in diameter by 610 mm (24 in.) in height, for shear strength testing (14). Approximately 68 to 73 kg (150 to 160 lb) of the limestone ballast material was poured into an aluminum split mold in four lifts and compacted using a 27.2-kg (60-lb) electric jackhammer for 4 s per lift. The compaction duration for each lift was selected to ensure that no particle breakage occurred during the compaction process. Approximate void ratio values of 0.68 were consistently achieved for the compacted specimens. Three layers of latex membrane, each 0.74 mm (0.029 in.) thick, were used to confine the specimen during testing. Two out of the three membranes were used during specimen compaction, and the third “seamless” membrane was used to ensure that the specimen was completely airtight. Aluminum O-rings were used to clamp the membranes against the top and bottom loading platens. Compressed air was used to apply target all-around confining pressures inside a 19-mm (0.75-in.) thick acrylic cylinder. Figure 2 shows a photograph



FIGURE 2 Photograph of compacted test specimen ready for shear strength testing.

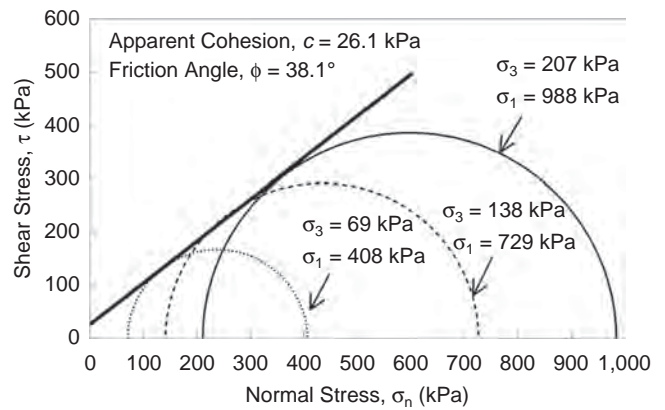


FIGURE 3 Mohr–Coulomb interpretation of limestone ballast shear strength tests (1 psi = 6.89 kPa).

of a compacted ballast specimen assembled inside the acrylic cylinder, ready for shear strength testing.

Monotonic triaxial shear strength tests were conducted by inducing a strain rate of 5% per second (30.5 mm/s ram movement for a 610-mm-high specimen) to the specimen at three confining pressure levels of 69, 138, and 207 kPa (10, 20, and 30 psi), respectively. Such high strain rates are considered to simulate the influence of traffic-induced high loading rates on railroad ballast behavior. A similar approach was proposed by Garg and Thompson to evaluate the shear strength properties of granular materials under vehicle loading (15). Past research has established that shear strength properties of ballast materials tested using the TX-24 setup are independent of the induced shear rate (16). Accordingly, this relatively faster shear rate (compared with the more conventional shear rate of 1% strain per minute) was used in this study to expedite the laboratory testing process. A LabVIEW-based data acquisition software was used to acquire the load (from an internal load cell mounted on the specimen) and deflection (from the internal linear variable differential transformer on the actuator) data during testing. Note that no additional on-specimen instrumentation for deflection measurement was used during the shear strength tests to prevent damage to the instrumentation components caused by excessive lateral deformation of the specimens during testing.

Figure 3 shows Mohr’s circle representations of the three shear strength tests conducted on unreinforced limestone ballast specimens at confining pressure levels of 69, 138, and 207 kPa, (10, 20, and 30 psi), respectively. The Mohr–Coulomb envelope captures the shear strength properties, cohesion intercept, and friction angle ϕ , as highlighted in Figure 3. Note that the ballast material tested comprised nonplastic fines, and therefore the apparent cohesion (intercept) value reported in Figure 3 is an outcome of linear interpretation of the nonlinear Mohr–Coulomb failure envelope.

DEM MODELING OF TRIAXIAL SHEAR STRENGTH TESTS

DEM is one of the most suitable numerical simulation approaches to simulate a granular system consisting of discrete particles. The DEM has already been successfully applied to simulate ballast behavior by using spherical elements or element clusters to represent ballast particles (17–19). The DEM simulation approach developed at the

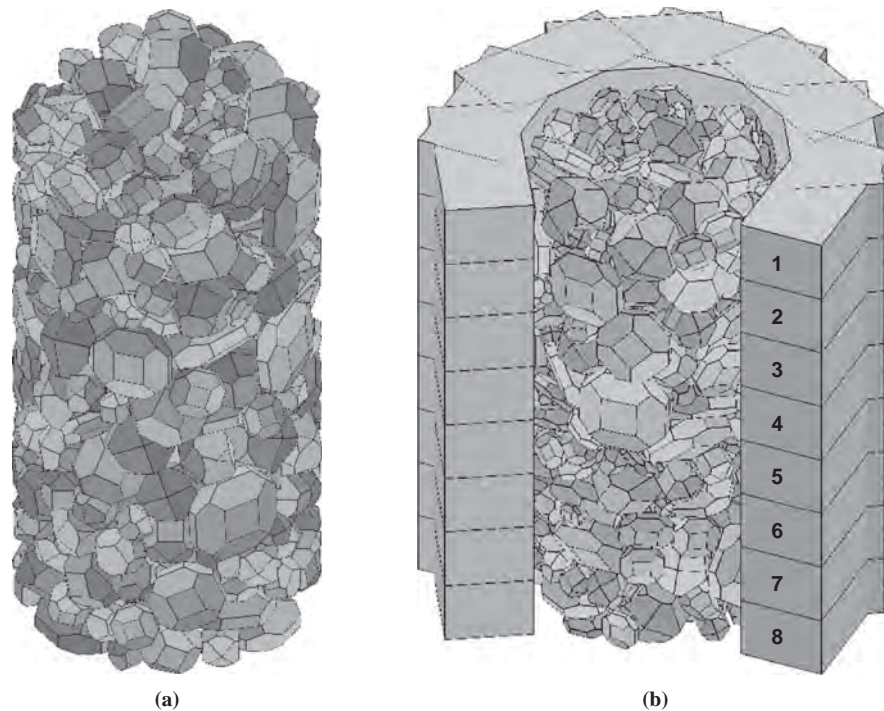


FIGURE 4 Ballast specimens: (a) DEM-generated cylindrical ballast specimen for triaxial testing and (b) cylindrical ballast specimen surrounded by simulated membrane layers. (The membrane layers are each 76 mm (3 in.) in length and are numbered 1 through 8 from top to bottom.)

University of Illinois adopts real polyhedral particles and has the capability to create actual ballast aggregate particles as 3-D polyhedron elements having the same particle size distributions and imaging-quantified average shape properties. This DEM approach was calibrated by the laboratory large-scale direct shear test results for ballast-size aggregate application (20) and has been successfully utilized to simulate complex ballast behavior, such as effects of multiscale aggregate morphological properties, gradation, and fouling (20–23). A successful field validation study was also completed to conclude that the DEM approach was quite adequate and reasonably accurate for predicting actual ballast layer deformation behavior (24).

Lee et al. used rigid rectangular cuboid discrete elements positioned in a cylindrical arrangement to simulate a flexible membrane with the BLOKS3D DEM program (25). Subsequently, Qian et al. used the BLOKS3D DEM program to simulate triaxial shear strength tests conducted on railroad ballast material (16). A similar approach was used in this study. A total of 96 rectangular cuboid discrete elements (in eight layers) were used to form a cylindrical chamber to confine the ballast specimen, as shown in Figure 4b. Each layer had 12 equal sized elements and the dimension of each single element was 20.3 cm (8 in.) long, 10.2 cm (4 in.) wide, and 7.6 cm (3 in.) high. These membrane elements were only allowed translational movement in a radial direction. Rotation and translation-type movements in other directions were restricted to replicate the deformation of the specimen membrane. To simulate the membrane behavior without applying extra confinement, the contact between membrane elements and the friction between the membrane elements and the ballast particles in contact were both ignored. The DEM simulations followed the same specimen preparation and loading steps of the laboratory tests. Further

details on the methodology adopted to simulate triaxial shear strength testing with DEM can be found elsewhere (16, 25).

The first task in this effort involved establishing DEM simulations of the triaxial monotonic shear strength tests conducted on the unreinforced limestone ballast specimens. Figure 5 shows the stress–strain curves obtained from the DEM simulations graphed together

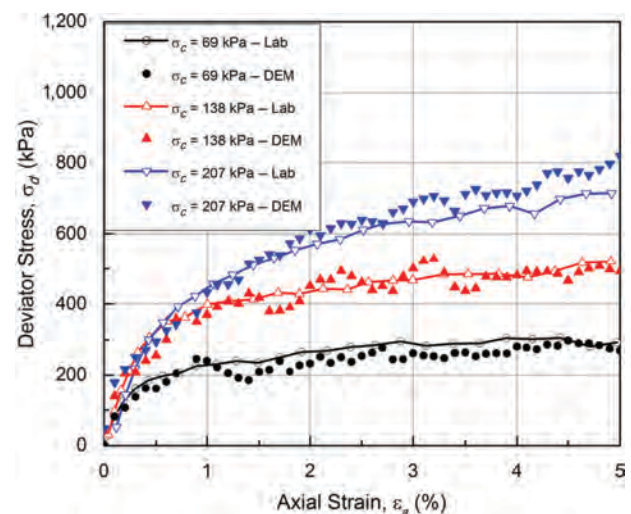


FIGURE 5 Stress–strain behavior of unreinforced limestone ballast specimens at three confining pressure levels obtained from laboratory testing and discrete element modeling (1 psi = 6.89 kPa).

with the experimental results. The method adopted for simulating the shear strength tests using DEM has been described in detail by Qian et al. (16). As clearly evident from Figure 5, the DEM method was successful in accurately predicting the stress–strain behavior of the limestone ballast specimens. To expedite the DEM simulation process, the comparison of laboratory and DEM results (presented in Figure 5) was presented only up to an induced axial strain level of 5%. Results of shear strength tests on geogrid-reinforced specimens, presented later in this paper, capture specimen stress–strain behavior up to induced axial strain levels of 10%.

As previously mentioned, the primary objective of this research effort was to identify the optimal position for geogrid reinforcement within a triaxial test specimen. This objective was accomplished by using the DEM simulation approach to monitor the lateral deformations induced in a triaxial test specimen during shear strength testing. As reported by Qian et al., using rigid rectangular cuboid discrete elements to simulate a flexible membrane helped to simulate triaxial shear strength tests and successfully capture the deformed shape of the specimen during testing (16). The effectiveness of geogrid reinforcement is primarily dependent on the degree of interlocking achieved between individual aggregate particles and the geogrid ribs and apertures (26). The benefits of geogrid reinforcement are therefore likely to be maximized under circumstances in which the aggregate particles would tend to displace laterally, thus mobilizing a high degree of interlocking between the geogrids and the particles. Accordingly, to optimize the geogrid placement along the specimen length, it is important to first analyze the amount of lateral displacement induced in a triaxial specimen at different positions along the specimen length. Placing the geogrid to “arrest” the maximum lateral displacement is therefore likely to mobilize the highest benefits from the geogrid reinforcement.

The lateral displacements during shearing at different locations along the specimen height were quantified by monitoring the average diameters corresponding to individual membrane layers (ML) in the DEM model. As already illustrated in Figure 4, the DEM simulation of the latex membranes used during triaxial testing involved 96 rigid rectangular cuboid discrete elements, each 76 mm (3 in.) high. The change in diameter at each ML corresponding to induced axial strain values induced during the shearing process is shown in Figure 6.

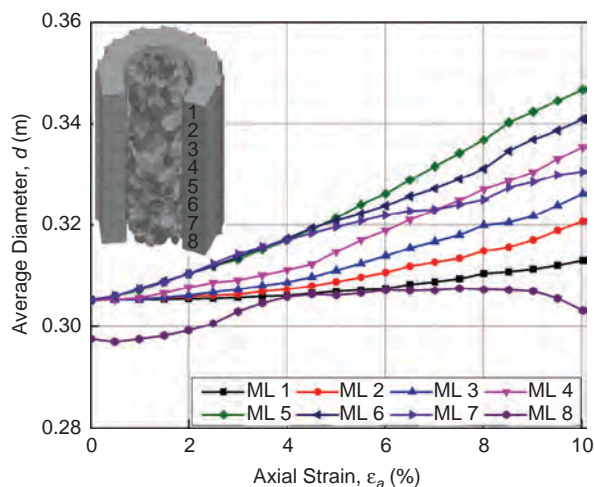


FIGURE 6 Changes in average diameter for eight membrane layers placed at different locations along specimen height with applied axial strain (ML = membrane layer).

ML 4, 5, and 6 exhibit the maximum lateral displacements during the shearing process. The lateral deformations corresponding to ML 1 and ML 8 shown in Figure 6 may not be representative and may reflect the effects of the specimen boundaries. For example, the ballast material confined by ML 1 will gradually move down with increasing axial strain, but ML 1 remains at the same vertical position. Therefore, with the gradual change in the specimen height caused by the induced axial strain, the entire height of ML 1 does not remain fully filled with ballast particles. Further, an increase in the axial strain level does not necessarily induce additional lateral deformation. Similarly, the bottom-most membrane layer (ML 8) may reflect the boundary effects caused by the rigid plate supporting the specimen. This effect is clearly reflected in Figure 6, which registers the two lowest average specimen diameter values for ML 1 and ML 8. Similar boundary effects are consistently observed during laboratory testing, with the top and bottom portions of the specimen undergoing minimal lateral deformations.

Close inspection of the results presented in Figure 6 indicates that the lateral deformation during shearing of a cylindrical ballast specimen is the highest near the specimen at midheight. Accordingly, geogrid placement at positions corresponding to ML 4, 5, and 6 is likely to result in the highest shear strength gains. Geogrid-reinforced triaxial specimens were therefore tested in the current study under five reinforcement configurations. These configurations represent different ratios between the depths of reinforcement (D_r) from the bottom of the loading plate and the loading plate diameter (B), which has been linked to the ultimate bearing capacity values (5). Including the unreinforced (control) case, results from the following six test configurations are presented below:

Configuration A. Unreinforced,

Configuration B. One geogrid placed at specimen midheight ($D_r/B = 1.0$),

Configuration C. One geogrid placed at 152 mm from the top of the specimen ($D_r/B = 0.5$),

Configuration D. One geogrid placed at 152 mm from the bottom of the specimen ($D_r/B = 1.5$),

Configuration E. Two geogrids placed at 152 mm from top and bottom of the specimen ($D_r/B = 0.5$, $D_r/B = 1.5$), and

Configuration F. Two geogrids placed at 254 mm from top and bottom of the specimen ($D_r/B = 0.83$, $D_r/B = 1.16$).

where

D_r = depth of geogrid from the bottom of loading plate and depth of bottom geogrid when two geogrids are placed,

B = diameter of loading plate (= 305 mm for the TX-24 test setup), and

D_t = depth of top geogrid from the bottom of loading plate.

TRIAXIAL SHEAR STRENGTH TESTING OF GEOGRID-REINFORCED BALLAST SPECIMENS

Geogrids Used

Two geogrid types with triangular- and square-aperture shapes were used in this study. Small pieces of the geogrid were cut to adequately fit within the aluminum split mold used for specimen preparation. Relevant dimensions and properties of the geogrids, as obtained from manufacturer specifications, are given in Table 1. Figure 7a shows the relative locations of geogrid placements corresponding to the different configurations listed above.

TABLE 1 Relevant Properties of Two Geogrid Types

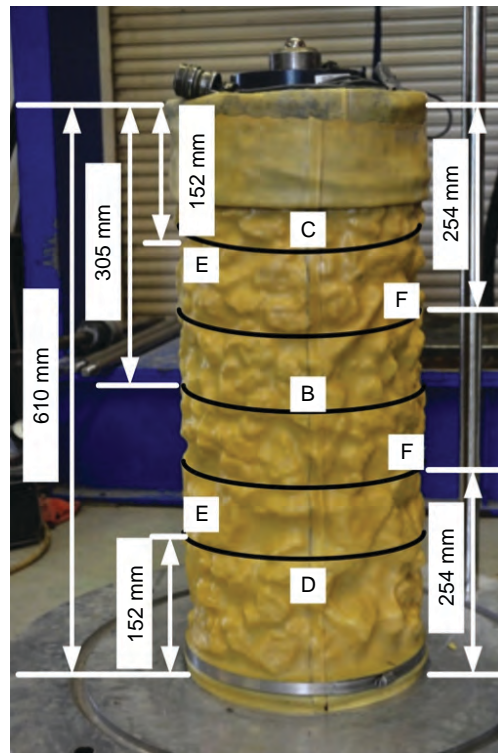
Property	Square Aperture, Side	Triangular Aperture	
		Longitudinal	Diagonal
Aperture dimensions (mm)	65	60	60
Ultimate QC strength (kN/m)	30	NA	NA
Junction efficiency (percentage)	NA	93	NA
Radial stiffness (kN/m @0.5% strain)	NA	350	NA

NOTE: QC = quality control; NA = not available.

Figure 7, *b* and *c*, shows photographs of the triangular-aperture and square-aperture geogrids, respectively.

Specimen Preparation for Triaxial Shear Strength Testing of Geogrid-Reinforced Ballast

The geogrid-reinforced specimens were prepared following a procedure similar to that used for preparing the unreinforced specimens. The thicknesses of each lift and corresponding compaction times were calculated on the basis of where geogrid was placed to ensure uniform and even compaction. Special care was taken to ensure proper penetration of the ballast particles into the geogrid apertures.



(a)



(b)



(c)

FIGURE 7 Photographs showing (a) relative locations of geogrid placement corresponding to test configurations, (b) triangular-aperture geogrid, and (c) square-aperture geogrid.

This procedure was done by hand placing the ballast particles within a 50-mm (2-in.) zone immediately below and above the geogrid and separately compacting this 100-mm (4-in.) zone encompassing the geogrid layer. At the end of placing all lifts and geogrid(s), each test specimen was checked for the total height and leveling of the top plate. The computed specimen void ratios (e) were consistently around 0.68, the same as unreinforced specimens. All shear strength tests for the geogrid-reinforced specimens were conducted at an all-around confining pressure level of 138 kPa (20 psi). Shearing rate was kept constant at 5% axial strain per second. At the end, the peak deviator stress values at failure were used to evaluate the geogrid reinforcement effects.

Figure 8 presents the peak deviator stress values at failure mobilized for the different reinforcement configurations for the triangular- and square-aperture geogrids. From the figure it is evident that Configuration F with two geogrids placed 254 mm (10 in.) from the top and bottom of the specimen achieved the highest shear strength properties for both geogrid types. Similarly, Configuration B

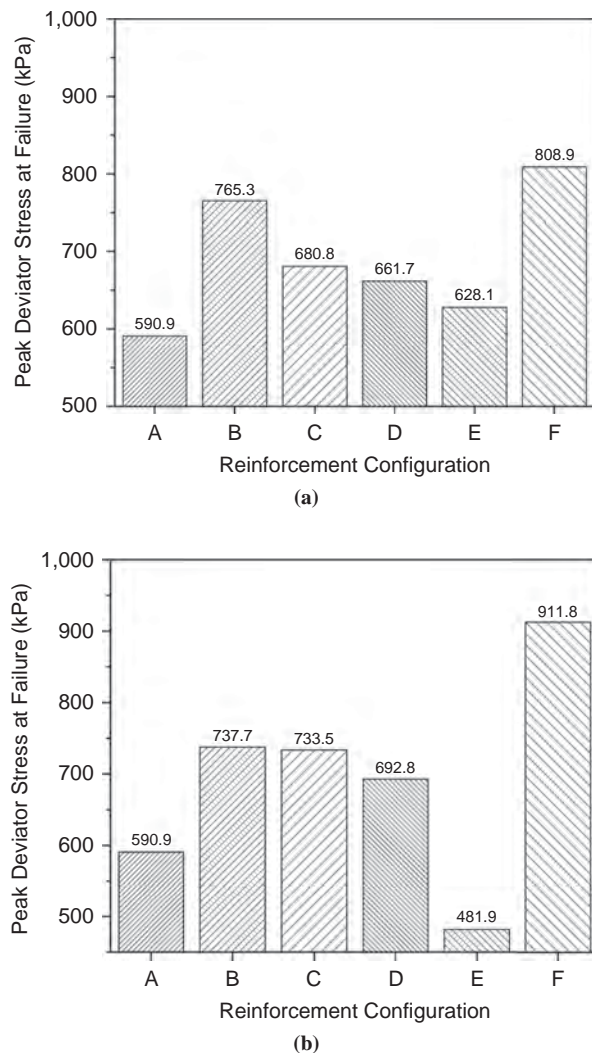


FIGURE 8 Comparative evaluation of peak deviator stress at failure corresponding to positions of geogrid along the specimen length: (a) triangular-aperture geogrid and (b) square-aperture geogrid.

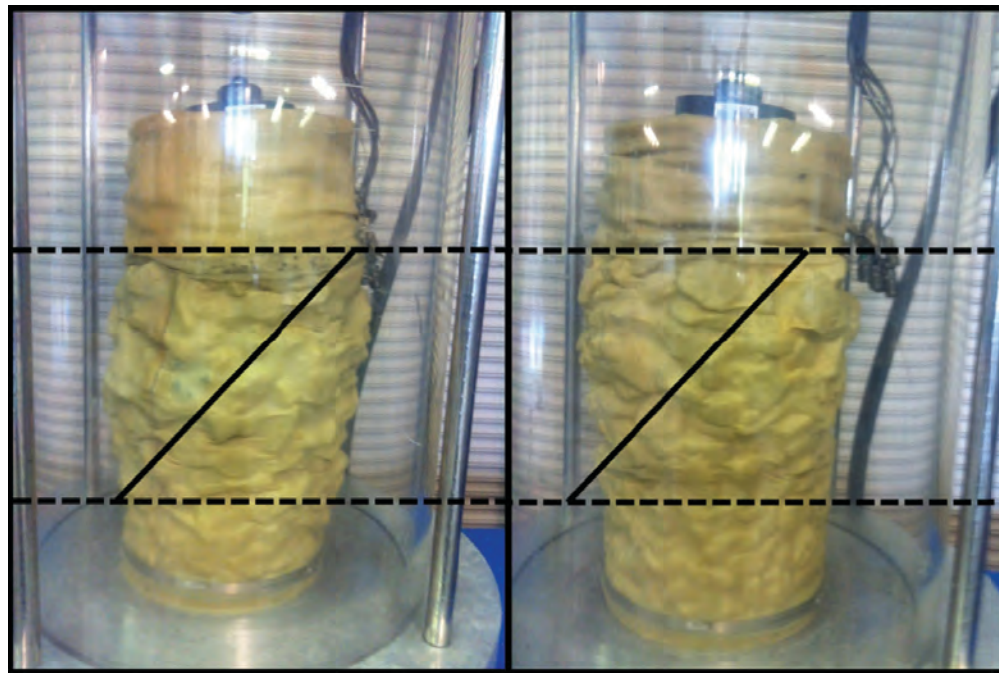
(one geogrid at specimen midheight) exhibited the second highest shear strength properties in both cases. Accordingly, it is evident that the addition of one extra layer of geogrid, and changing the placement along the specimen height, had a significant effect on the shear strength gain. This finding is in contradiction to results reported by Brown et al., who conducted a version of the plate loading test to report no significant difference in ballast settlement on changing the geogrid position in the ballast layer or by adding an extra layer of geogrid (2). Raymond and Ismail, on the contrary, observed an increase in the ultimate bearing capacity of an aggregate layer when an additional geogrid layer was placed (5). Figure 8a shows a minimal increase in the peak deviator stress at failure for Configuration E (two geogrids, 152 mm or 6 in. from top and bottom) compared with the unreinforced case (Configuration A). Figure 8b, however, shows a reduction in the peak deviator stress at failure for Configuration E compared with Configuration A. This phenomenon may potentially be linked to inadequate penetration of the ballast particles into the geogrid apertures. Brown et al. reported an increase in permanent deformation for specimens with small-aperture geogrids that resulted in improper penetration of the ballast particles into the geogrid aperture (2).

The lack of significant shear strength gain corresponding to Configuration E can further be justified by visually analyzing the location of the shear failure plane developed in the laboratory specimens. Figure 9a shows photographs of two deformed specimens after shear strength testing. The black dashed and solid lines in Figure 9a indicate the boundaries and shapes of the shear failure planes, respectively. The shear failure plane clearly develops near the specimen at midheight, whereas top and bottom portions of the specimen do not undergo significant lateral bulging. Accordingly, geogrid reinforcement is likely to be most beneficial when the shear failure plane intersects the reinforcement layer. This effect is ensured by placing the geogrid at the specimen at midheight (Configuration B) or 254 mm (10 in.) from the top and bottom of the specimen (Configuration F). When placed near the specimen ends (Configurations C, D, or E), geogrids are not likely to intersect the shear failure plane in the specimen and, therefore, they do not contribute much to shear strength gain. The evidence of this could be clearly observed by visually inspecting the geogrid ribs after testing.

Figure 9b shows a photograph of the square-shaped geogrid used in Configuration E after testing, whereas Figure 9c shows the picture after testing of a geogrid used in Configuration F. As clearly evident from both pictures, the geogrids used in Configuration F exhibit more damage to the ribs because they were placed within the shear failure plane.

DEM SIMULATIONS OF GEOGRID-REINFORCED TRIAXIAL TESTS

All shear strength tests conducted on the geogrid-reinforced specimens were numerically modeled using the DEM approach similar to that used for the unreinforced specimens. After first establishing the membrane elements, approximately 500 particles, having the same gradation and shape properties of the actual limestone ballast material, were poured into the cylinder in two or three sets. In between, a sheet of geogrid element was generated corresponding to the different reinforcement conditions being simulated. The geogrid element was modeled as a rigid nondeformable element with the same aperture dimensions as the geogrids used in the experimental study. However, the rib thickness of the square-aperture geogrid could not be accurately modeled using the DEM approach because



(a)



(b)



(c)

FIGURE 9 Photographs showing (a) deformed shapes of ballast specimen with indicated shear failure planes, (b) square-aperture geogrid after testing in Configuration E, and (c) square-aperture geogrid after testing in Configuration F.

the rib thickness for the square-aperture geogrid was significantly smaller than the individual ballast particle sizes. Modeling the exact rib dimensions of the square-aperture geogrid would significantly increase the required computational effort. The rib thickness for the square-aperture geogrid was therefore modeled in the current study as equal to that for the triangular-aperture geogrid. Accordingly, the DEM-simulated results for specimens with the square-aperture geogrids are likely to overestimate the deviator stress values compared with the laboratory test results owing to the relatively thicker rib thicknesses.

Figure 10 comparatively evaluates the DEM-simulated and experimental stress–strain behavior for specimens reinforced with the two geogrid types under Configurations B and F. Both the experimental and simulation data have been presented up to an

induced axial strain level of 10%. As shown in the figure, the DEM approach is able to accurately predict the stress–strain behavior of the specimens reinforced using the triangular-aperture geogrid. As expected, the DEM approach overestimates the deviator stress values for the specimens with the square-aperture geogrid, owing to the thicker rib thicknesses used in the simulations. The zigzag shapes of the experimental stress–strain curves at high axial strain levels indicate sudden strength drops. These drops can be attributed to the breaking of geogrid ribs and the resulting reorientation of aggregates from their previous interlocked positions. Immediately after this reorientation, the geogrid-reinforced ballast is restored to fully restrained condition as a result of the formation of new interlocked positions. This change leads to an increase in the specimen strength. Note that for the DEM approach, the geogrid elements are rigid,

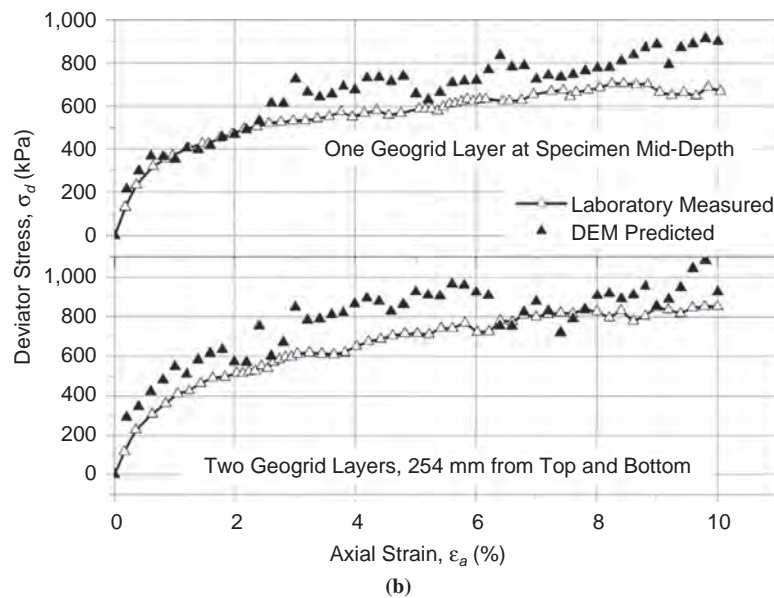
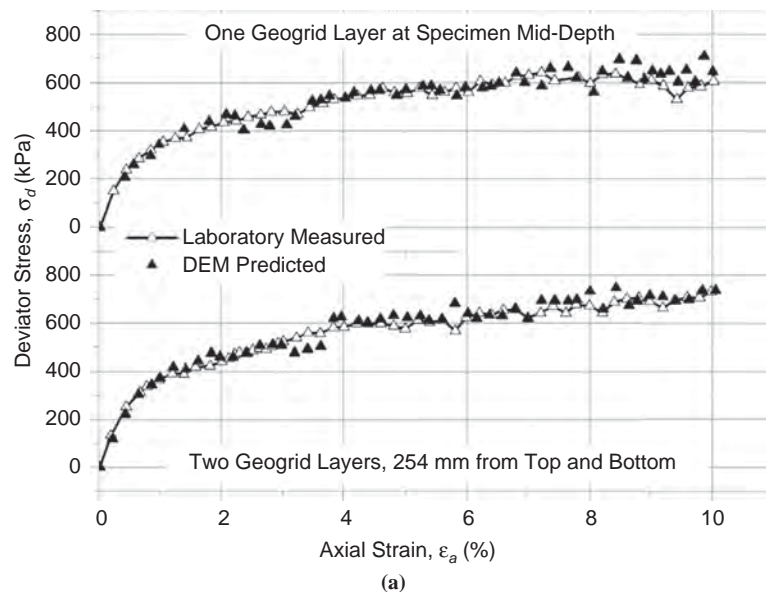


FIGURE 10 Deviator stress graphed with axial strain from laboratory testing and discrete element modeling of geogrid-reinforced ballast specimens: (a) triangular-aperture geogrid and (b) square-aperture geogrid.

nondeformable, and unbreakable. As the geogrids in the DEM simulation remain rigid, contact forces keep increasing between particles and geogrid ribs until particles overpass each other or geogrid ribs, which results in a large increase of strength before sudden strength drop. Therefore, the DEM simulation could overestimate the maximum strength of geogrid-reinforced ballast specimens. If more rib breakage was observed in the experiment, the overestimation in the DEM simulation would become more significant. As shown in Figure 10b, the maximum difference between the deviator stress values predicted by DEM simulations and measured from laboratory experiments were 213.5 and 305 kPa for specimens reinforced at middepth and 254 mm from top and bottom, respectively.

DISCUSSION ON RELEVANCE OF FINDINGS

The primary objective of this research effort was to identify the optimal position for geogrid placement in a cylindrical ballast test specimen for maximizing the shear strength. This objective was accomplished by conducting triaxial shear strength tests both through laboratory testing and numerical simulation. Data from both laboratory experiments as well as numerical simulations established that two geogrids placed 254 mm (10 in.) from top and bottom of the triaxial test specimen resulted in the maximum shear strength gain by reducing the lateral specimen bulging tendency. However, the failure mechanisms and the location of shear plane development within the cylindrical ballast test specimen may be significantly different from real track applications. Further research is needed before extending these findings directly to field applications.

SUMMARY AND CONCLUSIONS

This paper presents findings from an ongoing research study at the University of Illinois investigating the effects of geogrid reinforcement on ballast shear strength. An aggregate particle image-aided ballast modeling approach using the discrete element method was used to identify the optimal position for geogrid reinforcement in a cylindrical test specimen so that maximum shear strength gain could be achieved in a monotonic loading triaxial shear test. Specimens with five different reinforcement configurations were tested for shear strength properties using a large-scale triaxial test setup to evaluate the effectiveness of geogrid aperture shape and reinforcement depth. Placing two geogrids 254 mm (10 in.) from the top and bottom of the specimen resulted in the maximum shear strength gain for both triangular- and square-aperture geogrids. Such optimal placement of the geogrid ensures intersection of the developed shear failure plane by the reinforcement layer, thus preventing lateral bulging and ultimately leading to significant shear strength gains. The DEM simulations of the shear strength tests accurately captured the experimental ballast shear strength properties obtained in the laboratory from both the unreinforced and the geogrid-reinforced test specimens. Because the geogrid ribs were modeled as rigid and unbreakable elements and square-aperture geogrids could only be modeled with rather increased rib thicknesses, such geometric limitations of the geogrid discrete elements resulted in slight overestimations of the deviator stress values predicted by the DEM simulations when compared with the experimental findings. The DEM simulation platform currently being developed at the University of Illinois has the potential for further refinement in modeling to quantify individual effects of various geogrid properties, such as the aperture shape and size and

rib dimensions, on the aggregate assembly and, as a result, to improve manufactured geogrid product designs.

The primary contributions of the current research effort can be divided into three parts: (a) establish and quantify the benefits of geogrid reinforcement concerning ballast shear strength, (b) identify optimal locations for geogrid reinforcement within a cylindrical triaxial test specimen, and (c) establish the imaging-based DEM as a viable tool to adequately capture the effects of geogrid reinforcement on ballast shear strength. The findings presented in this paper have laid the path for subsequent research tasks that involve numerical simulation of real track geometries using the DEM modeling approach to compare the effects of geogrid placement at different depths. Results from such numerical simulations can subsequently be extended to implementation projects for real-life ballasted track applications.

ACKNOWLEDGMENTS

The authors acknowledge Jayhyun Kwon and Mark Wayne of Tensar International Corporation for providing the geogrids used in this research study. Development of the TX-24 test equipment was made possible through funds provided by BNSF Railway Company and the Transportation Technology Center, Inc. Special thanks are due to James Pforr for his help in conducting the laboratory experiments. The contributions of Anthony Mareno, Darold Marrow, Tim Prunkard, Marc Killion, and Michael Bletzinger during the design and manufacturing of the TX-24 components are greatly acknowledged. Finally, the authors thank the Illinois Center for Transportation for providing laboratory space for operation of the TX-24 test setup.

REFERENCES

1. Walls, J. C., and L. L. Galbreath. Railroad Ballast Reinforcement Using Geogrids. *Proceedings of Geosynthetics*, No. 87, 1987, pp. 38–45.
2. Brown, S. F., J. Kwan, and N. H. Thom. Identifying the Key Parameters That Influence Geogrid Reinforcement of Railway Ballast. *Geotextiles and Geomembranes*, Vol. 25, No. 6, 2007, pp. 326–335.
3. Bathurst, R. J., and G. P. Raymond. Geogrid Reinforcement of Ballasted Track. In *Transportation Research Record 1153*, TRB, National Research Council, Washington, D.C., 1987, pp. 8–14.
4. Shin, E. C., D. H. Kim, and B. M. Das. Geogrid-Reinforced Railroad Bed Settlement due to Cyclic Load. *Geotechnical and Geological Engineering*, Vol. 20, No. 3, 2002, pp. 261–271.
5. Raymond, G., and I. Ismail. The Effect of Geogrid Reinforcement on Unbound Aggregates. *Geotextiles and Geomembranes*, Vol. 21, No. 6, 2003, pp. 355–380.
6. Kwon, J., and J. Penman. The Use of Biaxial Geogrids for Enhancing the Performance of Sub-Ballast and Ballast Layers: Previous Experience and Research. Presented at 8th International Conference on Bearing Capacity of Roads, Railways and Airfields (BCR2A'09), Champaign, Ill., 2009.
7. Tutumluer, E., H. Huang, and X. Bian. Research on the Behavior of Geogrids in Stabilisation Applications. Presented at Jubilee Symposium on Polymer Geogrid Reinforcement Conference, London, 2009.
8. Qian, Y., J. Han, S. K. Pokharel, and R. L. Parsons. Stress Analysis on Triangular-Aperture Geogrid-Reinforced Bases over Weak Subgrade Under Cyclic Loading: An Experimental Study. In *Transportation Research Record: Journal of the Transportation Research Board*, No. 2204, Transportation Research Board of the National Academies, Washington, D.C., 2011, pp. 83–91.
9. Qian, Y., J. Han, S. K. Pokharel, and R. L. Parsons. Performance of Triangular Aperture Geogrid-Reinforced Base Courses over Weak Subgrade Under Cyclic Loading. *Journal of Materials in Civil Engineering*, Vol. 25, No. 8, 2013, pp. 1013–1021.
10. Dong, Y.-L., J. Han, and X.-H. Bai. Numerical Analysis of Tensile Behavior of Geogrids with Rectangular and Triangular Apertures. *Geotextiles and Geomembranes*, Vol. 29, No. 2, 2011, pp. 83–91.

11. McDowell, G. R., O. Harireche, H. Konietzky, S.F. Brown, and N.H. Thom. Discrete Element Modeling of Geogrid-Reinforced Aggregates. *Proceedings of the Institution of Civil Engineers*, Vol. 159, 2006, pp. 35–48.
12. Rao, C., E. Tutumluer, and J.A. Stefanski. Coarse Aggregate Shape and Size Properties Using a New Image Analyzer. *Journal of Testing and Evaluation*, Vol. 29, No. 5, 2001, pp. 461–471.
13. Rao, C., E. Tutumluer, and I.T. Kim. Quantification of Coarse Aggregate Angularity Based on Image Analysis. In *Transportation Research Record: Journal of the Transportation Research Board*, No. 1787, Transportation Research Board of the National Academies, Washington, D.C., 2002, pp. 117–124.
14. Mishra, D., H. Kazmee, E. Tutumluer, J. Pforr, D. Read, and E. Gehringer. Characterization of Railroad Ballast Behavior Under Repeated Loading: Results from New Large Triaxial Test Setup. In *Transportation Research Record: Journal of the Transportation Research Board*, No. 2374, Transportation Research Board of the National Academies, Washington, D.C., 2013, pp. 169–179.
15. Garg, N., and M.R. Thompson. Triaxial Characterization of Minnesota Road Research Project Granular Materials. In *Transportation Research Record 1577*, TRB, National Research Council, Washington, D.C., 1997, pp. 27–36.
16. Qian, Y., S. Lee, E. Tutumluer, Y.M.A. Hashash, D. Mishra, and J. Ghaboussi. Simulating Ballast Shear Strength from Large-Scale Triaxial Tests: Discrete Element Method. In *Transportation Research Record: Journal of the Transportation Research Board*, No. 2374, Transportation Research Board of the National Academies, Washington, D.C., 2013, pp. 126–135.
17. Lim, W.L., and G.R. McDowell. Discrete Element Modelling of Railway Ballast. *Granular Matter*, Vol. 7, No. 1, 2005, pp. 19–29.
18. Indraratna, B., P.K. Thakur, and J.S. Vinod. Experimental and Numerical Study of Railway Ballast Behavior Under Cyclic Loading. *International Journal of Geomechanics*, Vol. 10, No. 4, 2009, pp. 136–144.
19. Lu, M., and G.R. McDowell. Discrete Element Modelling of Railway Ballast Under Monotonic and Cyclic Triaxial Loading. *Géotechnique*, Vol. 60, No. 6, 2010, pp. 459–467.
20. Tutumluer, E., H. Huang, Y.M.A. Hashash, and J. Ghaboussi. Aggregate Shape Effects on Ballast Tamping and Railroad Track Stability. Presented at American Railway Engineering and Maintenance-of-Way Association Annual Conference, Louisville, Ky., 2006.
21. Tutumluer, E., H. Huang, Y.M.A. Hashash, and J. Ghaboussi. Discrete Element Modeling of Railroad Ballast Settlement. Presented at American Railway Engineering and Maintenance-of-Way Association Annual Conference, Chicago, Ill., 2007.
22. Tutumluer, E., W. Dombrow, and H. Huang. Laboratory Characterization of Coal Dust Fouled Ballast Behavior. Presented at American Railway Engineering and Maintenance-of-Way Association Annual Conference, Salt Lake City, Utah, 2008, pp. 21–24.
23. Tutumluer, E., H. Huang, Y.M.A. Hashash, and J. Ghaboussi. AREMA Gradations Affecting Ballast Performance Using Discrete Element Modeling (DEM) Approach. Presented at American Railway Engineering and Maintenance-of-Way Association Annual Conference, Chicago, Ill., 2009.
24. Tutumluer, E., Y. Qian, Y.M.A. Hashash, J. Ghaboussi, and D.D. Davis. Discrete Element Modelling of Ballasted Track Deformation Behavior. *International Journal of Rail Transportation*, Vol. 1, No. 1–2, 2013, pp. 57–73.
25. Lee, S.-J., Y.M.A. Hashash, and E.G. Nezami. Simulation of Triaxial Compression Test with Polyhedral Discrete Elements. *Computers and Geotechnics*, Vol. 43, 2012, pp. 92–100.
26. Koerner, R.M. *Designing with Geosynthetics*. Pearson Prentice Hall, Englewood Cliffs, N.J., 2005.

The Geosynthetics Committee peer-reviewed this paper.